

Fingerprinting the Hidden Facets of Plasmonic Nanocavities

Eoin Elliott¹, Kalun Bedingfield², Junyang Huang¹, Shu Hu¹, Bart De Nijs¹,
Angela Demetriadou^{2*}, Jeremy J Baumberg^{1*}

¹ NanoPhotonics Centre, Cavendish Laboratory, University of Cambridge, Cambridge CB3 0HE, UK.

² School of Physics and Astronomy, University of Birmingham, Edgbaston, Birmingham, B15 2TT, UK.

Abstract

The optical properties of nanogap plasmonic cavities formed by a NanoParticle-on-Mirror (NPoM, or patch antenna) are determined, across a wide range of geometric parameters including the nanoparticle diameter, gap refractive index, gap thickness, facet size and shape. Full understanding of the confined optical modes allows these nanocavities to be utilized in a wide range of experiments across many fields. Here, we show that the gap thickness t and refractive index n are spectroscopically indistinguishable, accounted for by a single gap parameter $G = n/t^{0.47}$. Simple tuning of mode resonant frequencies and strength is found for each quasi-normal mode, revealing a spectroscopic ‘fingerprint’ for each facet shape, on both truncated spherical and rhombicuboctahedral nanoparticles. This is applied to determine the most likely nanoscale morphology of facets hidden below each NPoM in experiment, as well as to optimize the constructs for different applications. Simple scaling relations are demonstrated, and an online tool for general use provided.

Keywords: plasmons, nanoparticle-on-mirror, patch antenna, quasi-normal modes, facet

Introduction

Confining light to the surface of plasmonic metals greatly increases light-matter interactions¹. This is further enhanced by plasmonic resonators which trap light in three dimensions, fueling advances in chemical² and biological³ sensing, non-linear optics⁴ and catalysis⁵. In contrast to microcavities which offer resonances with large quality factors Q but relatively large mode volumes V , plasmonic nanocavities leverage the evanescent nature of localized plasmons to squeeze light into deeply sub-wavelength volumes. As a consequence however, much of the optical energy is lost through inelastic scattering with the metal electrons, leading to low Q and small effective volume resonators. Because of this extreme localization and enhanced light-matter interaction, the spectral tuning and loss of trapped plasmonic modes is a subtle function of geometry at the nanometre scale. Understanding this interplay between nanoresonator geometry and light is vital in accounting for many widely used applications of plasmonic nanocavities such as enhancing exciton photoluminescence⁶, nonlinear vibrational pumping⁷, sensing, mid-infrared upconversion detectors⁸ or hot-electron emission⁹ among many others.

To understand the details of light fields in such plasmonic nanocavities, most previous works have relied on more cumbersome simulations of highly idealized geometries, and thus cannot easily account for the broad inhomogeneous distribution of scattering spectra observed from each nominally-identical construct¹⁰⁻¹². This prevents the development of deep understanding for many light-matter effects observed experimentally. For example, simple analytical predictions are even lacking as to how modes tune when the refractive index in the sub-wavelength volume changes, and how this might vary for differently shaped nanoparticles.

In this work, we examine several nanocavities formed by a truncated spherical NP and a rhombicuboctahedron-shaped NP to form a wide range of nanocavity shapes. These nanocavities support tightly trapped light and allow the role of lateral confinement upon their plasmonic modes to be explored. Light can be efficiently and robustly trapped as plasmons in nanogaps based on metal-insulator-metal (MIM) configurations, and here we take a scalable widely-used scheme based on the Nanoparticle-on-Mirror (NPoM) configuration¹³⁻¹⁸. Nanoparticles are inevitably faceted¹⁹, and thus form NPoMs with a MIM plasmonic nanogap of specific lateral shape. The influence of this nanocavity shape, as well as its material properties, are the focus of this work. We investigate structures consisting of a 10-200nm diameter metal nanoparticle (NP) spaced 0.5-10nm away from a metal mirror separated by a dielectric spacer, which is often of molecules or inorganic layers, but also polymers, perovskites, oxides or other materials²⁰. Although we focus here on NPoMs with both metal layers being Au (as this is the most robust commonly-used plasmonic material), all our findings develop analogously in other plasmonic metals such as Ag, Al and TiN. We also do not take into account the facet plane of the Au^{21,22}, because it would lead to systematic spectral shifts of only a few %, similar to other uncertainties (such as edge rounding, see below).

Usually, numerical analysis of plasmonic nanoresonators uses Finite Difference Time Domain or Finite Element Method simulations, solving Maxwell's equations with a specific incident E field or emitter location, chosen to replicate an experimental system under study²³. This however often obscures the underlying physics of the system and brings little physical intuition, necessitating a simulation for each experiment. To compensate, several semi-analytical models have emerged in recent years which qualitatively account for the dependence on parameters including NP diameter, facet size, gap refractive index and thickness²⁴⁻²⁶. These however suffer from limitations, such as multiple free fitting factors which are tuned to match the results of experiments carried out over limited parameter spaces. Additionally, they often only attempt to model the lowest energy NPoM resonance, and poorly account for higher-order modes. This is insufficient as higher-order modes are often responsible for excitation or emission (as in the case of photoluminescence). These 'dark' modes (which have an inherently higher Q) weakly scatter, and play a large role in light-matter strong coupling²⁷ and lasing²⁸, despite being typically disregarded. As the size, material, and shape (down to the nm-scale) significantly influence spectral tuning, isolating their effects in experiments can prove difficult²⁹.

Recently, the community has begun to leverage Quasi-Normal Mode (QNM) decomposition of the electromagnetic response of plasmonic resonators³⁰ including NPoMs³¹ to better understand their optical behaviour. These QNMs are eigen-solutions of Maxwell equations, producing a set of modes that are orthogonal, with parameters spanning eigenfrequencies $\tilde{\omega}$, quality factors \tilde{Q} , and mode volumes \tilde{V} . These parameters of the plasmonic resonators are complex, and since the modes lose substantial energy to Ohmic losses and radiate efficiently to the far-field, lead to low \tilde{Q} values. Physical quantities such as scattering cross-sections and Purcell enhancements can be constructed from a linear sum of these eigenmodes³². Understanding what influences these modes, and how their relative strengths contribute to physical phenomena, allows for a holistic understanding of the system. This is especially powerful when there are few QNMs in a spectral region of interest that can dominate the response observed³³, but they can also account for systems with many near-degenerate modes.

Here we find the solutions of > 2,000 QNMs over a variety of different geometric parameters. The results produce general trends that can predict the spectral position and intensity of the first 3 lowest order QNMs for all NPoM configurations, and provide a new benchmark for any further analytical models, as well as optimization conditions for designing nanoplasmonic cavities. Notably, while all

modes follow the qualitative trends of past works, they are found to quantitatively vary widely and distinguishably depending on the shape of the nanoparticle facet. Additionally, the effect of facet edge rounding, previously implicated as instrumental in the coupling of light out of the gap²⁶ is shown to affect QNMs differently. Finally, the results are compared to experimental measurements of mode positions to allow unique optical identification of the likely facet shape under each NP and its size.

Results & Discussion

We first explore the Truncated Sphere on Mirror (TSoM) which is commonly used to simulate NPoM geometries^{34–37} and consists of a sphere of diameter D truncated to produce a circular nanoparticle facet of diameter w , separated from a semi-infinite Au substrate by a dielectric gap of thickness t and refractive index n inside a surrounding background refractive index of 1 (Figure 1a, left). For a single combination of these parameters, the 145 lowest-energy QNMs of this system are computed by adapting the auxiliary-field eigenvalue formulation of [32] using Finite Element Methods, and categorized as lm by analogy to spherical harmonics Y_l^m , with the symmetries of their near-fields extracted at the mid-plane of the gap. Each computed eigenmode has a characteristic complex frequency $\tilde{\omega}_{lm} \equiv \omega_{lm} - i\kappa_{lm}$ consisting of real and imaginary components. A key feature of QNMs is that they can be used to reproduce the scattering spectrum, i.e. $E_s(\omega) = \sum_{lm} \alpha_{lm}(\omega) E_{lm}$, where $\alpha_{lm}(\omega)$ are frequency-dependent scattering coefficients³². These coefficients can be further factored into two parts, $\alpha_{lm} = S_{lm}(\omega)O_{lm}(\omega)$. The former term accounts for the lineshape of the mode scattering contribution to each peak at $\omega = \text{Re}[\tilde{\omega}_{lm}]$ and has a width proportional to $\text{Im}[\tilde{\omega}_{lm}]$ allowing us to reconstruct the scattering spectra (with asymmetries that arise from mode Fano interferences). The latter factor is a near non-dispersive term which accounts for the mode coupling to an incident field (see Supporting Information S1-2 for more detailed description). The real part of $\tilde{\omega}_{lm}$ is the spectral position of the QNM, while the imaginary component κ_{lm} gives the rate of the total energy loss from the mode (radiative and non-radiative), analogous to the decay rate of an emitter³². The non-radiative decay rate can also be independently calculated from the decay rate $\kappa_{MIM}(\omega, n, t)$ of a similar but non-radiative infinite MIM waveguide, for light at frequency $\omega = \text{Re}[\tilde{\omega}_{lm}]$ ³¹, as detailed in Supporting Information S2. Therefore, for each QNM, the radiative efficiency can be defined as

$$\eta_{lm} \equiv \frac{(\kappa_{lm} - \kappa_{MIM})}{\kappa_{lm}}. \quad (1)$$

This radiative efficiency η_{lm} is proportional to the scattering intensity of each QNM. The spectral response ($|E_s(\omega)|^2$) thus takes the form $|S_{lm}(\omega)|^2$, scaled by the radiative efficiency.

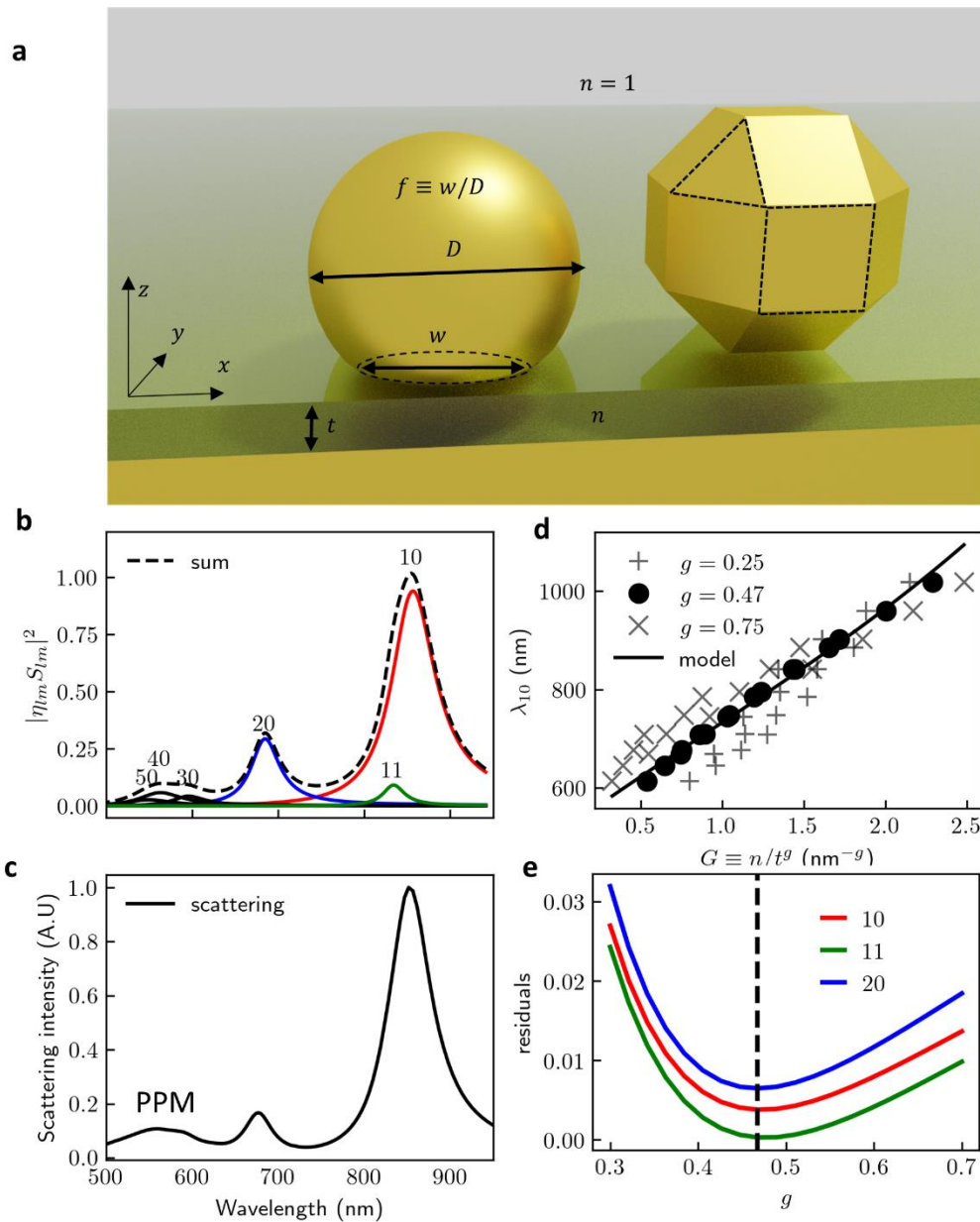


Fig. 1 | Simulation geometry and plasmon nanocavity modes. **a**, Schematic NPoM geometries used, built from Au NP separated from the Au semi-infinite plane by a dielectric gap of thickness t and refractive index n . (left) Truncated Sphere on Mirror (TSoM) of diameter D and circular facet diameter w . (right) Rhombicuboctahedron with square and triangular facets highlighted. **b**, Spectral response $|S_{lm}|^2$ of the six highest- η_{lm} QNMs, scaled by η_{lm}^2 , and their sum (dotted line). The 10,11, 20 modes are sufficient to reconstruct the spectral response beyond 600nm. Higher-order modes, most visibly the 30, 40, 50 modes, account for the ‘pseudo-mode’. **c**, Simulated scattering spectrum of TSoM. **d**, Wavelength of 10 QNM for TSoM with $D=80\text{nm}$ and $f \equiv w/D=0.3$ vs $G \equiv n/t^g$ for three values of g . Data become colinear for $g = 0.47$, line is 3rd degree polynomial regression fit. **e**, Sum of squared residuals of 3rd degree polynomial fits for $\lambda_{10}, \lambda_{11}, \lambda_{20}$ vs g for TSoM. Minimal residuals found at average $g = 0.472 \pm 0.004$.

The three most radiative modes ($lm = 10, 11, 20$) deliver most of the system’s scattering spectral response for $\lambda > 600\text{nm}$ (Fig.1b,c). As the wavelength approaches the surface plasmon resonance of

the isolated Au NP ($\sim 530\text{nm}$), the QNMs form a continuum of spectrally overlapping modes which are individually weakly scattering. This plasmon ‘pseudo-mode’³⁸ is poorly confined within the gap, and thus is largely uninfluenced by gap morphology, thickness and refractive index, instead depending almost entirely on the nanoparticle diameter D . For normally-incident excitation, a lateral dipole/multipole can be excited on the NP as a superposition of $l1$ modes in this mode-dense region. This linear sum of spectrally overlapping orthogonal QNM modes forms the weak ‘transverse mode’ for the system.

Adding more modes does not significantly alter the spectrum, affirming the power of the QNM approach to understand plasmonic nanoantennae - phenomena can be understood using a few dominant modes in the spectral region of interest. For most NPoM applications, these are the 10, 11, and 20 modes, which are thus the focus here. Dependences of higher-order modes, such as the 21 and 22 modes are presented in Supporting Information Fig. S2 where calculated.

Parameter	Set of values				unit
$f = w/D$	0.15	0.3	0.46	0.6	
D - diameter	40	60	80	100	nm
t - gap size	0.75	1.5	3.0	6.0	nm
n - refractive index	1.25	1.5	1.75	2.0	

Table 1 | Parameter sweeps. $f \equiv w/D$ is the relative facet size with respect to the nanoparticle diameter, D is nanoparticle diameter, t is gap thickness, and n is gap refractive index.

A parametric sweep is performed for the TSoM geometry using all combinations of the parameters shown in Table 1, extracting the handful of lowest-energy QNMs for each combination of values. When the calculated mode wavelengths λ_{lm} are plotted against the scaled gap parameter $G \equiv n/t^g$, they become collinear for $g = 0.47$ (demonstrated for the 10 mode in Figure 1d with $f = 0.3$, $D = 80\text{nm}$). This shows that the dimensionality of the problem can be reduced, and that gap refractive index and thickness cannot be distinguished.

Instead of scaling with optical path $2nDf$ (as for microcavities or interferometers), these metal-insulator-metal waveguides support a plasmon with $\lambda_{\text{eff}} = \pi t |\text{Re}\epsilon_m|/n^2$ for small t . Using a Drude model $\epsilon_m = \epsilon_\infty - \lambda^2/\lambda_p^2$ gives the quasi-analytical formula for 10 mode wavelength described in ²⁰,

$$\lambda_{10} \simeq \lambda_p \sqrt{\frac{w n^2}{\alpha_l t} + \epsilon_\infty} \quad (2)$$

showing indeed a dependence as $n/t^{0.5}$ is expected beyond $\lambda > 600\text{nm}$. Clearly this simple 1D model has to be corrected for 2D confinement, non-circular facets, and leakage beyond the facet edges, but gives a good intuition of the full simulations.

Performing 3rd degree polynomial regression (see Supporting Information S5-6) on λ_{10} , λ_{11} , λ_{20} with f , D , and G as regressors, a minimum residual is found when $g = 0.472 \pm 0.004$. Similar behaviour is found for square and triangular facets of the rhombicuboctahedral geometry (described below), resulting in minima at $g = 0.467 \pm 0.006$ and 0.465 ± 0.006 respectively. The average of all these, $g = 0.47$ is used throughout the rest of this work. Our key conclusion here is that gap refractive index and thickness cannot be independently extracted from spectroscopy.

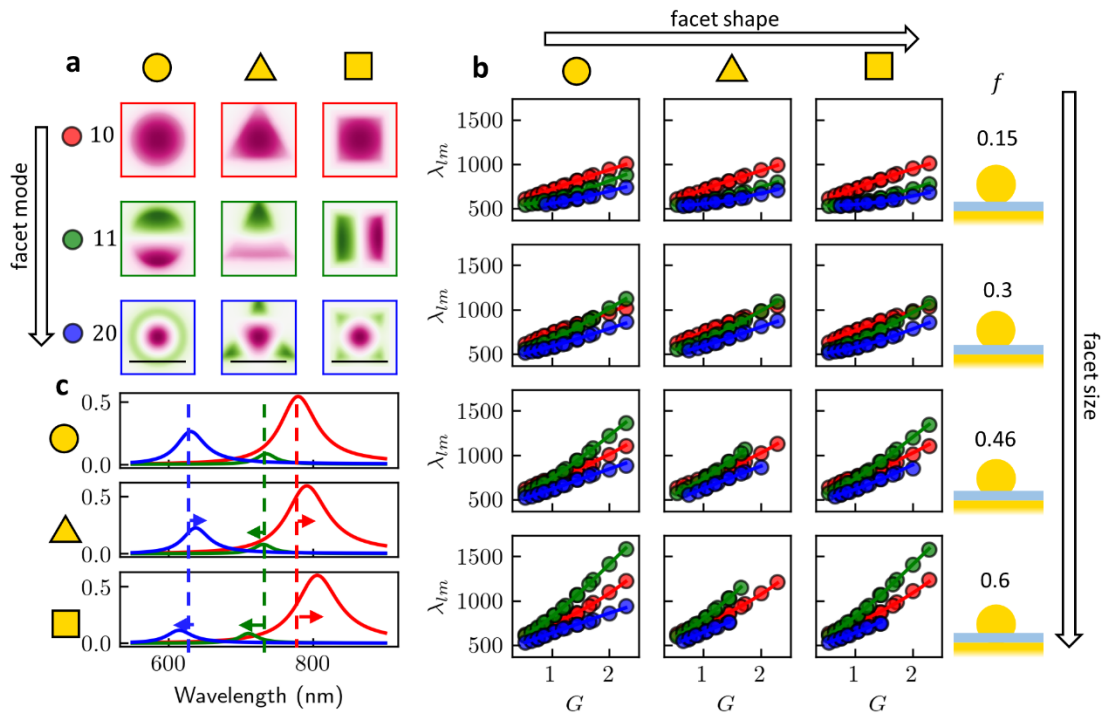


Fig. 2 | Effect of facet shape and size. **a**, Near-field E_z extracted in the middle of the gap for 10, 11, 20 modes (rows), for circular, triangular and square facets (columns), for $D=80\text{nm}$, $f=0.3$, $t=1.5\text{nm}$, $n=1.5$. Scalebar on bottom row is 25nm. All facets have the same area. **b**, QNM wavelength λ_{lm} for each facet shape (columns), facet fraction (rows), and mode (colour), for the $D = 80\text{nm}$ subset of the simulated parameter space. Solid lines are polynomial regression fits to the full parameter space. **c**, QNM scattering response for 10, 11, 20 modes (red, green, blue) of circular, triangular and square facets, for same parameters.

To investigate the effect of facet shape on the QNMs of NPoMs, a rhombicuboctahedral nanoparticle is used since it is one of several common Au nanoparticle shapes observed³⁵ and has either the triangular or square facets (outlined in Fig. 1a) assembled on the mirror. The facet sizes are increased by slicing the volume (similarly as for TSoMs, although it slightly truncates the facet corners) and decreased by extending the faces adjacent to the facet. The side-length and facet side length are defined to preserve the cross-sectional area and ratio of cross-sectional area to facet area (respectively) of that of a TSoM defined by f and D . For a given f , D , the area of a circular, square or triangular facet is thus the same, as well as the NP cross-sectional area. For a ‘regular’ rhombicuboctahedron (unaltered bottom facet) the regular facet fraction $f_r \approx 0.3$ for the triangular facet, and for the square facet $f_r \approx 0.46$ (see Supporting Information S3).

The near-field E_z maps of 10, 11 and 20 modes (Figure 2a) show how the electric field profiles in the gap change with the NP facet shape. As rotational symmetry is still preserved, the two 11 modes remain always degenerate and orthogonal, so the orientation of its nodal line in the near-field is arbitrary (a new pair of 11 modes can be constructed from a sum of any previous orthogonal pair). As most of the electric field is confined within the facet centre for the 10 mode, it is relatively unperturbed by gap morphology. The 11 modes however are located near the edges, implying that as facet size f increases, they are more perturbed, red-shifting their resonant frequencies. The presence of a radial antinode in the 20 mode near the edge of the facet also suggests it has a strong dependence on both f and G , since whether this node is within the gap affects its behaviour strongly.

For each geometry and combination of parameters in Table 1, the lowest energy QNMs are extracted. Using polynomial regression, the spectral positions are found to be very well predicted with low-order polynomials for the 10 mode with a circular facet. While the 10 mode is well predicted using 2nd degree polynomials, higher-order modes require 3rd degree regression. Polynomials for each geometry and mode are provided in Supporting Information S5-6, and are a key result of this work. The 10,20 modes tune far less with f than $m \neq 0$ modes, particularly 11. For this reason, identifying the 11 position is highly desirable to determine facet size f spectroscopically (see below).

The $D = 80\text{nm}$ subset of this data with polynomial fits (Figure 2b) shows the expected trends of mode wavelength increasing with f , D , and n , and decreasing with t . The λ_{11} resonance increases more rapidly with increasing f than λ_{20} , which in turn increases more rapidly than λ_{10} , as implied by their near-field profiles (as discussed above). Higher-order modes such as 22 and 33, whose near-field profiles resemble 2D whispering gallery modes and are thus localized at the facet edges, also redshift disproportionately quickly with increasing f, D . In fact, for large portions of the parameter space, we find that $\lambda_{11} > \lambda_{22} > \lambda_{10}$ (see Supporting Information Fig. S3). Subtle changes in λ_{lm} between the three facet shapes can be observed, for instance with $D=80\text{nm}$, $f=0.3$, $t=1.5\text{nm}$, $n=1.5$ (Fig.2c). Arrows show how the dominant modes shift differently compared to the TSoM as the facet shape changes (despite the imposed facet area conservation), delivering ‘shape fingerprints’ in the NPoM scattering spectrum (see below).

The radiative efficiency η_{lm} depends on f, D, t and n in a very systematic way. Comparing the imaginary vs real parts of the complex mode frequencies $\tilde{\omega}_{lm}$ (loss vs tuning, Figure 3a) with the non-radiative MIM mode (dashed line) for the same parameters shows how it matches the non-radiative modes. Using Eqn. (2) thus allows the radiative efficiencies to be compared across modes. We see that η_{10} depends only on D and λ_{10} (Fig. 3b), and is more emissive than the higher-order modes (Fig.3c,d). For each D , the 10 mode radiates best at a specific wavelength λ_{ant} , corresponding to the antenna response of the system. This antenna radiative rate scales $\propto D^3$ as expected from the NP polarizability. The antenna frequency regime is consistent with previous analytical models analysing the NPoM in terms of its equivalent circuit (Fig. 3e)²⁴ (see Supporting Information Fig. S5). The weak dependence on f is likely due to the decreasing total volume of the NP when truncation increases.

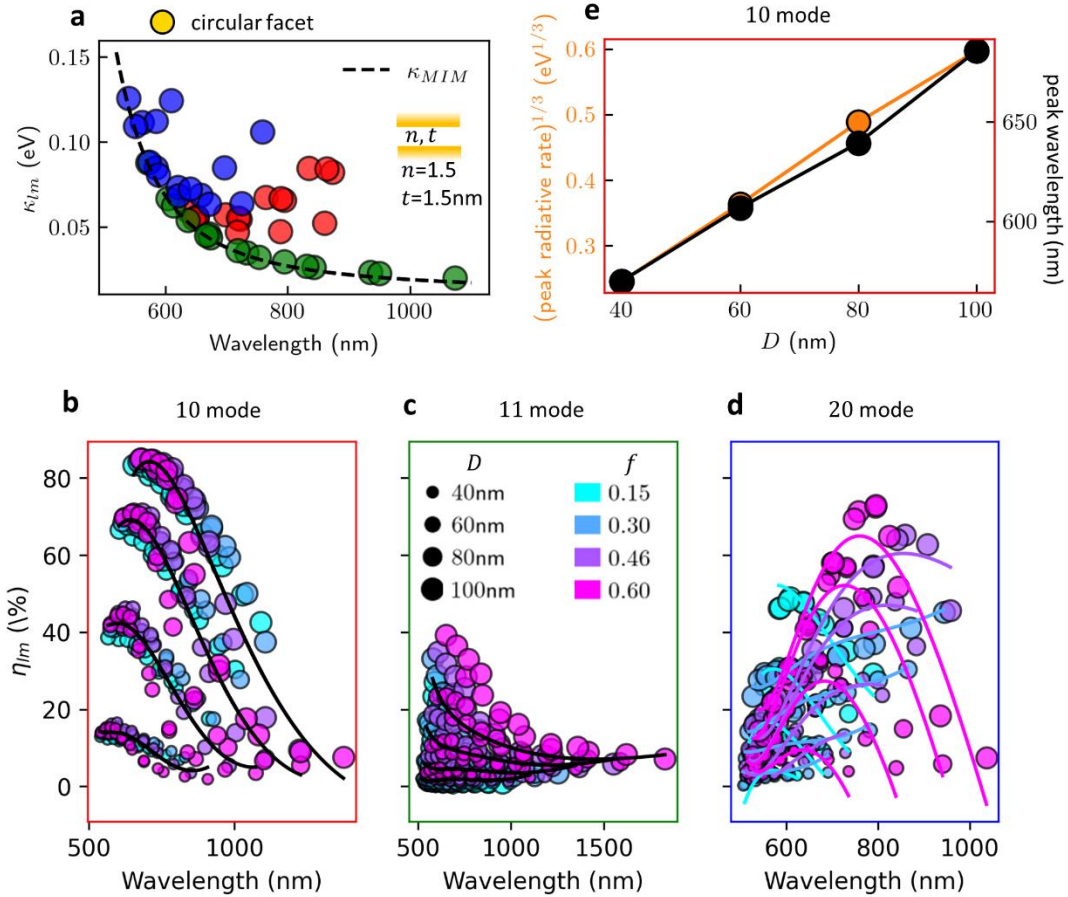


Fig. 3 | Radiative efficiency of modes. **a**, Imaginary component (κ_{lm}) of QNM frequency vs λ_{lm} for $n=1.5$, $t=1.5$ nm QNMs, together with $\kappa_{MIM}(\lambda, n, t)$ of non-radiative MIM waveguide dispersion (for same gap parameters, dashed line). Only 10 (red) and 20 (blue) modes are radiative (lie above line) compared to 11 modes (green). **b-d**, Radiative efficiency η_{lm} vs λ_{lm} of (b) 10, (c) 11 and (d) 20 modes for circular facet. Black lines show polynomial regressor using D , λ_{lm} , coloured lines for η_{20} also incorporate f . Crosses in (b) show radiative peak λ_{ant} . **e**, Cubed root of peak radiative rate vs NP diameter D (orange) demonstrating D^3 antenna scaling, and peak radiative wavelength λ_{ant} for 10 mode from (b), vs D .

When the 10 plasmonic nanocavity mode frequency coincides with this antenna frequency, scattering is maximized. The analysis also shows that the 11 mode becomes more radiative for large t and small n (small G) at short wavelengths (Fig. 3c), because the 11 mode near-field then extends outside of the facet area. In these circumstances, it couples more effectively to excitation fields, radiating vertically (normal to the mirror), however when the 11 mode is within the facet area this vertical radiation is suppressed. The behaviour of η_{20} is strongly affected by facet fraction f as well as D , λ_{lm} . This is due to the proximity of the radial antinode with the facet edge, with the radiative efficiency becoming significantly poorer when this antinode encounters the facet edge itself. This becomes clearer when separating η_{20} for each D comparing the circular, square and triangular facets (Supporting Information Fig. S6). These observations suggest that the facet edges can be highly important in selecting which modes are possible to couple to. We thus now explore a further geometrical parameter, the rounding of this facet edge.

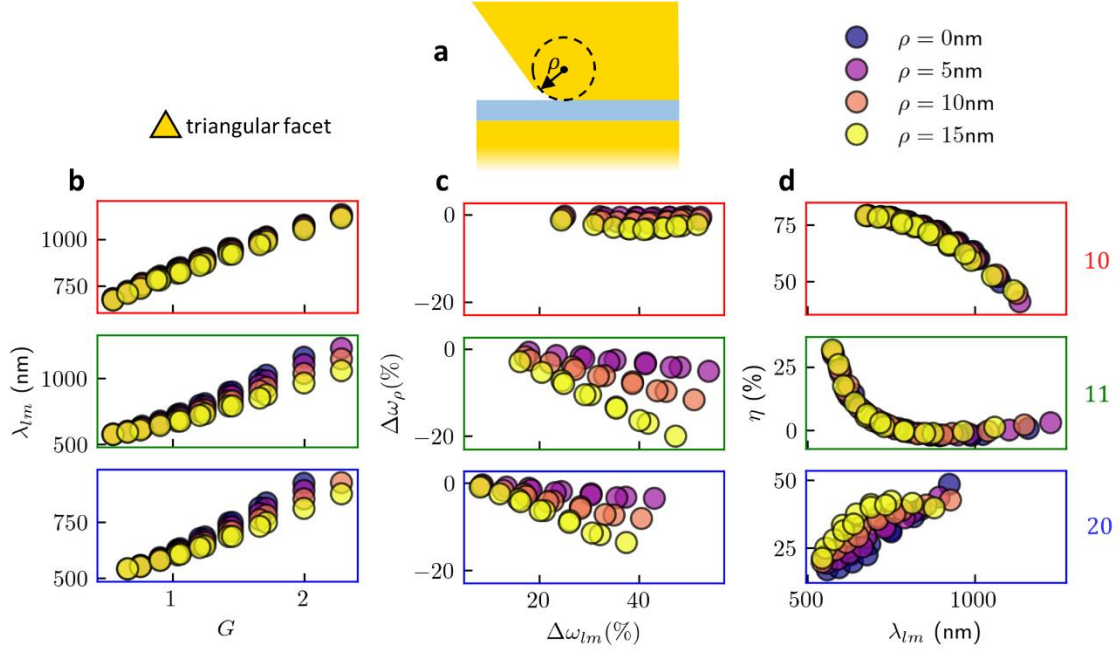


Fig. 4 | Effect of rounding the facet edge. **a**, Schematic of facet rounding parameter ρ , the radius used to fillet the bottom facet. **b**, λ_{lm} vs gap coupling parameter G for $lm = 10, 11, 20$ (red, green, blue bordered plots), $D = 80\text{nm}$, $f \simeq 0.3$. Edge rounding has little effect on 10 mode. **c**, Fractional frequency shift of ω_{lm} due to edge rounding $\Delta\omega_\rho \equiv (\omega_{lm,\rho} - \omega_{lm,\rho=0})/\omega_{lm,\rho=0}$, plotted against fractional frequency shift of ω_{lm} from the isolated NP resonance, $\Delta\omega_{lm} \equiv (\omega_{NP} - \omega_{lm,\rho})/\omega_{NP}$, highlighting how the effect of rounding is proportional to the coupling to the mirror. **d**, η_{lm} vs λ_{lm} shows little dependence of radiative coupling on edge rounding.

The rounding radius ρ of the filleted NP bottom (triangular) facet edge is varied ($D = 80\text{nm}$, $f \simeq 0.3$). For all modes, the effect of rounding increases as gap parameter G increases (tighter optical confinement). The effect of edge rounding is found to be proportional to the frequency difference $\Delta\omega_{lm}$ between the isolated NP resonance and the NPoM lm plasmon mode. In all cases, rounding the edges blueshifts the modes from the unrounded case ($\Delta\omega_\rho$) because the effective size of the facet is decreased. This blue-shifting increases with G since the modes are more strongly localized under the facet edge, increasing its influence. This effect is stronger for the 11 and 20 modes, as their fields are more localized at the facet edge, with $\Delta\omega_{11} > 20\%$ at $\rho = 10\text{nm}$ for high G . By contrast, for the 10 mode at high G , $\Delta\omega_\rho$ decreases because the high confinement causes the 10 mode profile to retract from the facet edges, outcompeting any rounding effect. The shifts and relative magnitudes caused by increasing ρ correlate with the dependence on decreasing f , $\Delta\omega_{11} > \Delta\omega_{20} > \Delta\omega_{10}$, indicating that the dominant effect of increasing ρ is decreasing the facet area, and as such is well accounted for by the facet size f .

The change in radiative efficiency is found to be small for the 10 and 11 modes (Fig. 4d). This implies that intuitive ideas based on the nanocavity plasmon E field leaking around the facet edge depending on its rounding are incorrect. Previous work suggested that the facet edge angle was also important²⁶, but is not evidenced for the 10 mode (Fig. 3b). There is however a stronger effect on the 20 mode, as the radial antinode is near the facet edge.

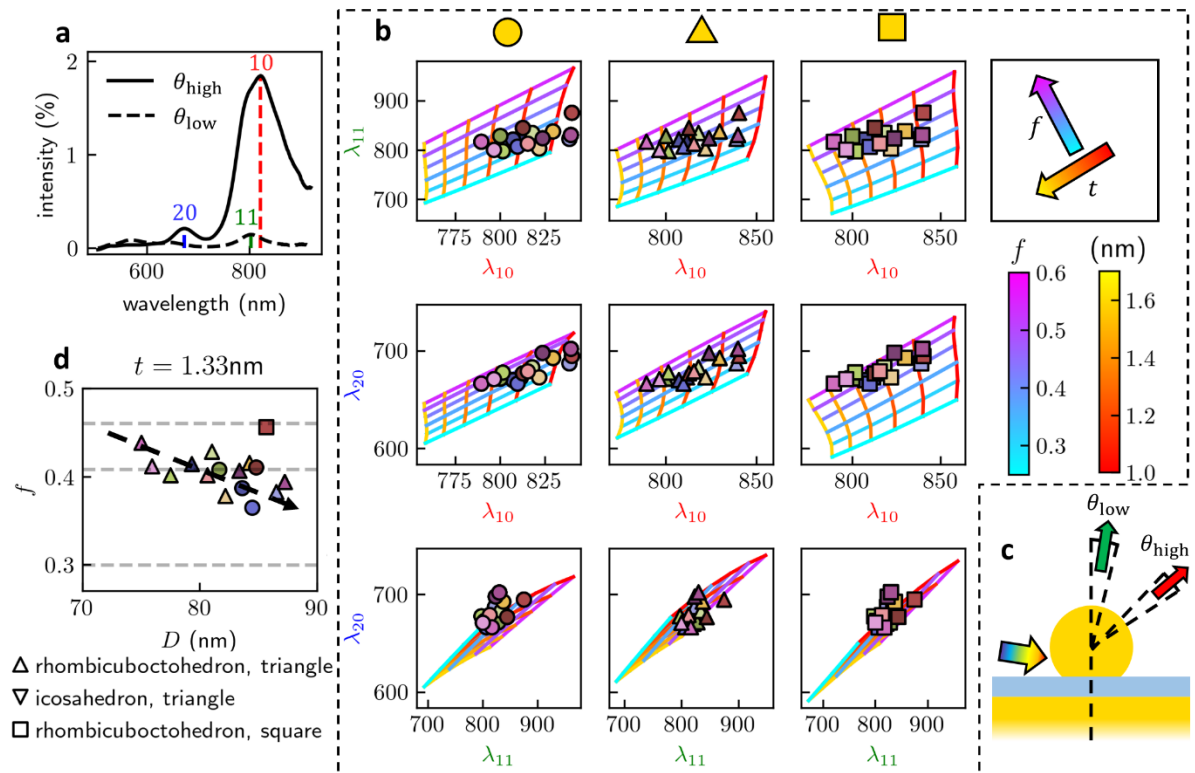


Fig. 5 | Fingerprinting experimental spectra. **a**, Experimental white-light high-angle (θ_{high}) and low-angle (θ_{low}) single NPoM scattering spectra. Mode positions of 10, 20 extracted from former, 11 from latter. **b**, Correlations between λ_{lm} for 10, 11, 20 modes plotted for 17 measured NPoMs. For each facet geometry (columns), the relationship between each mode pair is mapped from polynomial fits: plotted vs t for a range of f (blue-purple lines) and vice versa (red-yellow lines). The three correlations should identify similar (f, t), and best agreement is seen for triangular facets (centre column). **c**, Schematic of high- and low-angle collection of scattering. **d**, Most-probable facet shape (marker shape) for each NP vs their extracted f, D . Horizontal lines correspond to the facet sizes f for platonic NP shapes, indicating many NPs are likely triangular faceted with $f \approx 0.4$. This corresponds to either annealed rhombicuboctahedron facets, or perfect icosahedron facets.

High-angle (θ_{high}) and low-angle (θ_{low}) white-light scattering spectra are taken of 17 NPoMs with a bi-phenylthiol (BPT) gap spacer molecular layer ($n \sim 1.5$, $t \sim 1.3 \text{ nm}$), by angularly-separating the collected light (see Methods). A typical example (Figure 5a) shows that as expected the 10, 20 modes radiate primarily at high angles, while the 11 mode radiates along the normal to the mirror, as previously shown in NPoMs²⁰. This angular decomposition separates the $\sim 800 \text{ nm}$ spectral peak into the overlapping 10 and 11 modes, which we show is highly desirable for assigning a facet shape.

For visualization purposes, the refractive index n is fixed at 1.45 and NP diameter D at 82 nm (see below). Changing D tunes all modes similarly within reasonable polydispersities ($80 \pm 10 \text{ nm}$) of our samples and thus has little explanatory power (see Supporting Information Fig. S7a). While n and t may be combined without loss of information into the gap coupling parameter G (Fig. 1d), here we use t (nm) for easy comprehension. To visualize the information in the cross-correlations of the three measured mode positions, the polynomial fits of the 10, 11, 20 mode wavelengths for each facet shape are plotted on 10 vs 11, 10 vs 20 and 11 vs 20 graphs (Fig. 5b). In each, we fix the facet f and vary gap size t (and vice versa), allowing the set of each NPoM peaks to unambiguously predict a value of (f, t) for each geometry. The agreement between (f, t) for these three correlations is a measure of how likely this simulated facet shape is the one probed in experiment. The data points

coincide at similar parameter values for the triangular facet (Fig. 5b, centre column), suggesting most NPoMs have triangular Au(111) facets face down.

By allowing free variation of f , D , t and minimising the residuals across the different facet shapes (see Supporting Information Fig. S5b), we find that most NPoMs have triangular facets, with average $\bar{D} = 82 \pm 5 \text{ nm}$ and $\bar{t} = 1.4 \pm 0.3 \text{ nm}$. This \bar{D} matches well with the expected 80 nm NP size. Previous ellipsometry measurements suggested that similarly prepared BPT SAMs have thickness $t = 1.3 \text{ nm}$ and refractive index $n = 1.45$ ³⁹, agreeing well with these optimized parameters.

Since the gaps are well defined in these robust samples, $G \equiv n/t^{0.47}$ does not vary from NPoM to NPoM, and n, t are thus fixed to investigate the correlation of f and D (Fig. 5d). Triangular faceted NPoMs (12 out of the 17) have f clustered around 0.4–0.5, indicating that their facets are relatively large (the circular facets are rather similar). This might be attributed to facet growth/annealing of rhombicuboctahedral facets, (regular rhomboctahedra have $f_r \simeq 0.3$), however more likely is for icosahedra consisting entirely of triangular facets for which $f_r = 0.408$, or cuboctahedra for which $f_r = 0.47$. This accounts well for the prevalence of triangular facets assigned. Typically, all these shapes of particles can be identified in electron microscope images, as well as less frequent pentagonal bipyramids^{35,40} The inverse correlation between f and D , (dashed arrow Fig. 5d) is also expected, as faceting generally increases with decreasing metal radius, with surface energy terms becoming more relevant. The full analysis of the three lowest wavelength plasmons observed in the NPoMs thus allows us to extract detailed parameters for their nanoscale morphologies.

A key highlight here is thus the experimental confirmation of facet size and shape based on theoretical simulations (provided in an online tool) and experimental spectra. These have previously been causing confusion in many experimental papers from diverse researchers. Despite predictions of our analytic analysis, the gap scaling was not seen in previous simulations because they were not accurate enough, while not being obvious to any intuition.

Conclusion

We show how 3D morphology influences plasmonic nanocavity modes. By employing improved computational methods, detailed information can be now extracted about heterogeneous ensembles on a construct-by-construct basis. More specifically, we show that a handful of QNMs dominate the spectral response of NPoMs, and these tune widely with geometrical parameters. Their resonant frequency dependence on the gap parameters (refractive index n and width t) can be described entirely in terms of a composite gap parameter $G \equiv n/t^{0.47}$, and low-order polynomials of D , f and G . The radiative efficiency of the dominant mode scales in intensity and spectral position as for a classical antenna, depending only on spectral position and D . Finally, angle-dependent spectroscopy isolates ‘dark’ modes in experimental scattering spectra from NPoMs. Using the lowest three modes in comparison with simulated results allows likely facet shapes to be assigned as mostly triangular. The insights from this analysis support a wide range of experiments which employ ultralow volume plasmonic cavities, providing their mode spectrum and its sensitivity to geometry at the nm-scale. This underpins a wide variety of applications that utilize these nanocavities.

Online App

To aid the reader, we provide an online app (see <https://www.np.phy.cam.ac.uk/npom-calculator>) which gives the mode positions and estimated scattering spectra for any combination of the above parameters, as well as refer to the full parameter sets in the online supplementary data. Since the three-dimensional nanoparticle shape above the facet has much less effect on the modes (mainly the height controls the antenna resonance λ_{ant}), this model works for every typical NPoM shape. The source python code is freely accessible. We note that the same QNMs are also found in

nanoparticle dimers, but experimentally the overlap of the two touching facets is uncontrolled, leading to very widely heterogeneous tuning ranges compared to the NPoM (as expected from the influence of f above).

Methods

Finite Element Method simulations were performed with COMSOL adapting the QNMEig toolkit [24]. A multi-pole Lorentz-Drude model was used to model $\varepsilon_{Au}(\omega)$, necessary for the augmented-field formulation of QNM decomposition.

$$\varepsilon_{Au}(\omega) = \varepsilon_{\infty} \left(1 - \frac{\omega_{p,1}^2}{\omega^2 - \omega_{0,1}^2 + i\gamma_1\omega} - \frac{\omega_{p,2}^2}{\omega^2 - \omega_{0,2}^2 + i\gamma_2\omega} \right)$$

$\varepsilon_{\infty} = 6$, ε_0 , $\omega_{p,1} = 5.37 \times 10^{15}$ rad/s, $\omega_{0,1} = 0$ rad/s, $\gamma_1 = 6.216 \times 10^{13}$ rad/s, $\omega_{p,2} = 2.636 \times 10^{15}$ rad/s, $\omega_{0,2} = 4.572 \times 10^{15}$ rad/s, and $\gamma_2 = 1.332 \times 10^{15}$ rad/s. These parameters were obtained by fitting to Johnson and Christy Au⁴¹. This data and the fit are presented in Supporting Information S10. Where background fields are required, a TM plane wave incident on the same structure without the NP is simulated with periodic boundary conditions.

All simulated geometries have 5nm rounding applied to the bottom facet only. A quarter geometry and appropriate symmetry was used to reduce the computational time for TSoMs. With accurate search regions for the QNMs and careful choice of meshing, the full set of simulations takes a week with 15 cores on COMSOL.

NPoM samples were prepared on Template-stripped Au, fabricated by established methods⁴². A Biphenyl-4-Thiol (BPT) (Sigma-Aldrich, 97%) SAM was formed by submerging the substrate in a 1 mM solution in anhydrous ethanol (Sigma-Aldrich, < 0.003% H₂O) for 24h, then rinsing with ethanol. 80nm Au NPs (BBI solutions) were then dropcast on the surface.

Individual NPoMs are illuminated with focused incoherent white light (halogen lamp) source at an annular illumination angle of 64–75° with respect to normal incidence, and scattered light with an angle of <64° is collected through a dark-field objective (Olympus 100xBD, NA 0.9). The scattering pattern from a NPoM is determined using the light intensity distribution at the back focal plane of the microscope objective. Single NPoM structure is spatially isolated by spatially filtering the real image plane with a pinhole. The back focal plane image is demagnified by 3 times before being imaged on the entrance slit (150 μm wide) of a Triax 320 spectrometer, where a narrow range of the scattering pattern near $k_x/k_0 = 0$ is filtered and dispersed by a 150 l/mm grating and collected using an Andor Newton 970 BVF EMCCD.

Acknowledgements

We thank Rohit Chikkaraddy for fruitful discussions, and Nuttawut Kongsuwan for technical consultation.

Funding Sources

JJB acknowledges EPSRC grants EP/N016920/1, EP/L027151/1, NanoDTC EP/L015978/1, and EU THOR 829067, POSEIDON and PICOFORCE. AD gratefully acknowledges support from the Royal Society University Research Fellowship URF\R1\180097, Royal Society Research Fellows Enhancement Award RGF \EA\181038, Royal Society Research grants RGS \R1\211093 and funding from EPSRC for the CDT in Topological Design EP/S02297X/1.

Author Contributions

All authors developed the simulations and models, all authors contributed to writing the manuscript.

Conflicts of interest

The authors declare no conflicts of interest.

Corresponding authors

Correspondence to J.J.B. (jjb12@cam.ac.uk), A.D. (a.demetriadou@bham.ac.uk).

Data availability

Data for all the figures are available online at <https://doi.org/10.17863/CAM.86416>.

References

- (1) Maier, S. A. *Plasmonics: Fundamentals and Applications*; Springer US: New York, NY, 2007.
- (2) De Nijs, B.; Carnegie, C.; Szabó, I.; Gryns, D. B.; Chikkaraddy, R.; Kamp, M.; Barrow, S. J.; Readman, C. A.; Kleemann, M. E.; Scherman, O. A.; Rosta, E.; Baumberg, J. J.; Li, R. Q.; Hernáizgomez-Pérez, D.; García-Vidal, F. J.; Fernández-Domínguez, A. I. Inhibiting Analyte Theft in Surface-Enhanced Raman Spectroscopy Substrates: Subnanomolar Quantitative Drug Detection. *ACS Sensors* **2019**, *4* (11), 2988–2996.
- (3) Jiang, J.; Wang, X.; Li, S.; Ding, F.; Li, N.; Meng, S.; Li, R.; Qi, J.; Liu, Q.; Liu, G. L. Plasmonic Nano-Arrays for Ultrasensitive Bio-Sensing. *Nanophotonics* **2018**, *7* (9), 1517–1531.
- (4) Panoiu, N. C.; Sha, W. E. I.; Lei, D. Y.; Li, G.-C. Nonlinear Optics in Plasmonic Nanostructures. *J. Opt.* **2018**, *20* (8), 083001.
- (5) Brongersma, M. L.; Halas, N. J.; Nordlander, P. Plasmon-Induced Hot Carrier Science and Technology. *Nat. Nanotechnol.* **2015**, *10* (1), 25–34.
- (6) Liu, W.; Lee, B.; Naylor, C. H.; Ee, H. S.; Park, J.; Johnson, A. T. C.; Agarwal, R. Strong Exciton-Plasmon Coupling in MoS₂ Coupled with Plasmonic Lattice. *Nano Lett.* **2016**, *16* (2), 1262–1269.
- (7) Tomita, K.; Kojima, Y.; Kannari, F. Selective Coherent Anti-Stokes Raman Scattering Microscopy Employing Dual-Wavelength Nanofocused Ultrafast Plasmon Pulses. *Nano Lett.* **2018**, *18* (2), 1366–1372.
- (8) Xomalis, A.; Zheng, X.; Chikkaraddy, R.; Koczor-Benda, Z.; Miele, E.; Rosta, E.; Vandenbosch, G. A. E. E.; Martínez, A.; Baumberg, J. J. Detecting Mid-Infrared Light by Molecular Frequency Upconversion with Dual-Wavelength Hybrid Nanoantennas. *Science (80-.)*. **2021**, *374* (6572), 1268–1271.
- (9) Li, W.; Valentine, J. G. Harvesting the Loss: Surface Plasmon-Based Hot Electron Photodetection. *Nanophotonics* **2017**, *6* (1), 177–191.
- (10) Funston, A. M.; Novo, C.; Davis, T. J.; Mulvaney, P. Plasmon Coupling of Gold Nanorods at Short Distances and in Different Geometries. *Nano Lett.* **2009**, *9* (4), 1651–1658.
- (11) Talley, C. E.; Jackson, J. B.; Oubre, C.; Grady, N. K.; Hollars, C. W.; Lane, S. M.; Huser, T. R.; Nordlander, P.; Halas, N. J. Surface-Enhanced Raman Scattering from Individual Au Nanoparticles and Nanoparticle Dimer Substrates. *Nano Lett.* **2005**, *5* (8), 1569–1574.
- (12) Osberg, K. D.; Rycenga, M.; Harris, N.; Schmucker, A. L.; Langille, M. R.; Schatz, G. C.; Mirkin, C. A. Dispersible Gold Nanorod Dimers with Sub-5 Nm Gaps as Local Amplifiers for Surface-

- Enhanced Raman Scattering. *Nano Lett.* **2012**, *12* (7), 3828–3832.
- (13) Barik, P.; Pal, S.; Pradhan, M. On-Demand Nanoparticle-on-Mirror (NPoM) Structure for Cost-Effective Surface-Enhanced Raman Scattering Substrates. *Spectrochim. Acta - Part A Mol. Biomol. Spectrosc.* **2021**, *263*, 120193.
 - (14) Cuartero-González, A.; Fernández-Domínguez, A. I. Dipolar and Quadrupolar Excitons Coupled to a Nanoparticle-on-Mirror Cavity. *Phys. Rev. B* **2020**, *101* (3), 1–15.
 - (15) Devaraj, V.; Jeong, H.; Kim, C.; Lee, J.-M.; Oh, J.-W. Modifying Plasmonic-Field Enhancement and Resonance Characteristics of Spherical Nanoparticles on Metallic Film: Effects of Faceting Spherical Nanoparticle Morphology. *Coatings* **2019**, *9* (6), 387.
 - (16) Huh, J. H.; Lee, J.; Lee, S. Comparative Study of Plasmonic Resonances between the Roundest and Randomly Faceted Au Nanoparticles-on-Mirror Cavities. *ACS Photonics* **2018**, *5* (2), 413–421.
 - (17) Qi, X.; Lo, T. W.; Liu, D.; Feng, L.; Chen, Y.; Wu, Y.; Ren, H.; Guo, G. C.; Lei, D.; Ren, X. Effects of Gap Thickness and Emitter Location on the Photoluminescence Enhancement of Monolayer MoS₂ in a Plasmonic Nanoparticle-Film Coupled System. *Nanophotonics* **2020**, *9* (7), 2097–2105.
 - (18) Huynh, L. T. M.; Lee, S.; Yoon, S. Formation, Stability, and Replacement of Thiol Self-Assembled Monolayers as a Practical Guide to Prepare Nanogaps in Nanoparticle-on-Mirror Systems. *Bull. Korean Chem. Soc.* **2019**, *40* (8), 839–842.
 - (19) Marks, L. D.; Peng, L. Nanoparticle Shape, Thermodynamics and Kinetics. *J. Phys. Condens. Matter* **2016**, *28* (5), 053001.
 - (20) Baumberg, J. J.; Aizpurua, J.; Mikkelsen, M. H.; Smith, D. R. D. R. D. R. Extreme Nanophotonics from Ultrathin Metallic Gaps. *Nat. Mater.* **2019**, *11* (7), 668–678.
 - (21) Yang, Y.; Zhu, D.; Yan, W.; Agarwal, A.; Zheng, M.; Joannopoulos, J. D.; Lalanne, P.; Christensen, T.; Berggren, K. K.; Soljačić, M.; Agrawal, A.; Zheng, M.; Joannopoulos, J. D.; Lalanne, P.; Christensen, T.; Berggren, K. K.; Soljačić, M. A General Theoretical and Experimental Framework for Nanoscale Electromagnetism. *Nature* **2019**, *576* (7786), 248–252.
 - (22) Rodríguez Echarri, A.; Gonçalves, P. A. D.; Tserkezis, C.; García de Abajo, F. J.; Mortensen, N. A.; Cox, J. D. Optical Response of Noble Metal Nanostructures: Quantum Surface Effects in Crystallographic Facets. *Optica* **2021**, *8* (5), 710.
 - (23) Said, A.; Atia, K. S. R.; Obayya, S. S. A. On Modeling of Plasmonic Devices: Overview. *J. Opt. Soc. Am. B* **2020**, *37* (11), A163.
 - (24) Benz, F.; de Nijs, B.; Tserkezis, C.; Chikkaraddy, R.; Sigle, D. O.; Pukenas, L.; Evans, S. D.; Aizpurua, J.; Baumberg, J. J. Generalized Circuit Model for Coupled Plasmonic Systems. *Opt. Express* **2015**, *23* (26), 33255.
 - (25) Sigle, D. O.; Mertens, J.; Herrmann, L. O.; Bowman, R. W.; Ithurria, S.; Dubertret, B.; Shi, Y.; Yang, H. Y.; Tserkezis, C.; Aizpurua, J.; Baumberg, J. J. Monitoring Morphological Changes in 2D Monolayer Semiconductors Using Atom-Thick Plasmonic Nanocavities. *ACS Nano* **2015**, *9* (1), 825–830.
 - (26) Tserkezis, C.; Esteban, R.; Sigle, D. O.; Mertens, J.; Herrmann, L. O.; Baumberg, J. J.; Aizpurua, J. Hybridization of Plasmonic Antenna and Cavity Modes: Extreme Optics of Nanoparticle-on-Mirror Nanogaps. *Phys. Rev. A - At. Mol. Opt. Phys.* **2015**, *92* (5), 1–6.

- (27) Chikkaraddy, R.; De Nijs, B.; Benz, F.; Barrow, S. J.; Scherman, O. A.; Rosta, E.; Demetriadou, A.; Fox, P.; Hess, O.; Baumberg, J. J. Single-Molecule Strong Coupling at Room Temperature in Plasmonic Nanocavities. *Nature* **2016**, *535* (7610), 127–130.
- (28) Ojambati, O. S.; Arnardottir, K. B.; Lovett, B. W.; Keeling, J.; Baumberg, J. J. Few-Emitter Lasing in Single Ultra-Small Nanocavities. **2021**, 1–13.
- (29) Ahmed, A.; Banjac, K.; Verlekar, S. S.; Cometto, F. P.; Lingenfelder, M.; Galland, C. Structural Order of the Molecular Adlayer Impacts the Stability of Nanoparticle-on-Mirror Plasmonic Cavities. *ACS Photonics* **2021**, *8* (6), 1863–1872.
- (30) Lalanne, P.; Yan, W.; Vynck, K.; Sauvan, C.; Hugonin, J. P. Light Interaction with Photonic and Plasmonic Resonances. *Laser Photonics Rev.* **2018**, *12* (5), 1–38.
- (31) Kongsuwan, N.; Demetriadou, A.; Horton, M.; Chikkaraddy, R.; Baumberg, J. J.; Hess, O. Plasmonic Nanocavity Modes: From Near-Field to Far-Field Radiation. *ACS Photonics* **2020**, *7* (2), 463–471.
- (32) Yan, W.; Faggiani, R.; Lalanne, P. Rigorous Modal Analysis of Plasmonic Nanoresonators. *Phys. Rev. B* **2018**, *97* (20), 1–10.
- (33) Wu, T.; Gurioli, M.; Lalanne, P. Nanoscale Light Confinement: The Q's and V's. *ACS Photonics* **2021**, *8* (6), 1522–1538.
- (34) Chikkaraddy, R.; Baumberg, J. J. Accessing Plasmonic Hotspots Using Nanoparticle-on-Foil Constructs. *ACS Photonics* **2021**, *8* (9), 2811–2817.
- (35) Benz, F.; Chikkaraddy, R.; Salmon, A.; Ohadi, H.; De Nijs, B.; Mertens, J.; Carnegie, C.; Bowman, R. W.; Baumberg, J. J. SERS of Individual Nanoparticles on a Mirror: Size Does Matter, but so Does Shape. *J. Phys. Chem. Lett.* **2016**, *7* (12), 2264–2269.
- (36) Devaraj, V.; Lee, J. M.; Adhikari, S.; Kim, M.; Lee, D.; Oh, J. W. A Single Bottom Facet Outperforms Random Multifacets in a Nanoparticle-on-Metallic-Mirror System. *Nanoscale* **2020**, *12* (44), 22452–22461.
- (37) Huang, Y.; Ma, L.; Li, J.; Zhang, Z. Nanoparticle-on-Mirror Cavity Modes for Huge and/or Tunable Plasmonic Field Enhancement. *Nanotechnology* **2017**, *28* (10), 105203.
- (38) Li, R. Q.; Hernáñez-Pérez, D.; García-Vidal, F. J.; Fernández-Domínguez, A. I. Transformation Optics Approach to Plasmon-Exciton Strong Coupling in Nanocavities. *Phys. Rev. Lett.* **2016**, *117* (10), 1–5.
- (39) Ganbold, E. O.; Joo, S. W. Raman Spectroscopy of Biphenyl-4,4'-Dithiol and p-Terphenyl-4,4''-Dithiol on Gold Surfaces. *Bull. Korean Chem. Soc.* **2015**, *36* (3), 887–890.
- (40) Kamp, M.; de Nijs, B.; Kongsuwan, N.; Saba, M.; Chikkaraddy, R.; Readman, C. A.; Deacon, W. M.; Griffiths, J.; Barrow, S. J.; Ojambati, O. S.; Wright, D.; Huang, J.; Hess, O.; Scherman, O. A.; Baumberg, J. J. Cascaded Nanooptics to Probe Microsecond Atomic-Scale Phenomena. *Proc. Natl. Acad. Sci. U. S. A.* **2020**, *117* (26), 14819–14826.
- (41) Johnson, P. B.; Christy, R. W. Optical Constants of the Noble Metals. *Phys. Rev. B* **1972**, *6* (12), 4370–4379.
- (42) Hegner, M.; Wagner, P.; Semenza, G. Ultralarge Atomically Flat Template-Stripped Au Surfaces for Scanning Probe Microscopy. *Surf. Sci.* **1993**, *291* (1–2), 39–46.

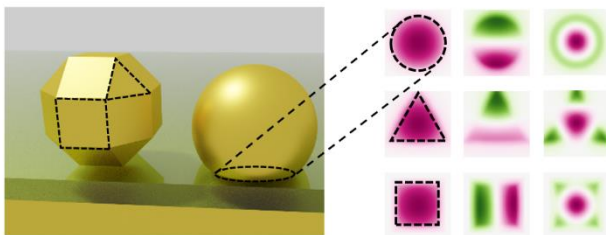
For Table of Contents Use Only

Fingerprinting the Hidden Facets of Plasmonic Nanocavities

Eoin Elliott¹, Kalun Bedingfield², Junyang Huang¹, Shu Hu¹, Bart De Nijs¹,
Angela Demetriadou^{2*}, Jeremy J Baumberg^{1*}

¹ NanoPhotonics Centre, Cavendish Laboratory, University of Cambridge, Cambridge CB3 0HE, UK.

² School of Physics and Astronomy, University of Birmingham, Edgbaston, Birmingham, B15 2TT, UK.



Left: Schematic of Nanoparticle on Mirror and possible facet shapes. Right: effect of facet shape on QNM near-field in the gap.

Supporting Information

Description:

Relating QNMs to scattering: Details of how QNM complex frequencies can be related to scattering intensity

Radiative efficiency of QNMs: Its motivation, definition and description

Simulation Geometry: Exact details of the simulation geometry, in particular the NP facet.

QNM wavelengths mapped across parameter space: All simulated QNMs, and their polynomial fits.

Polynomial regression terms: Information necessary to reconstruct the polynomial fits for oneself.

Influence of f on QNMs: Exploration of how the facet size affects modes differently.

Radiative efficiencies for each facet geometry: All radiative efficiencies, and their fits.

Assigning facet shapes and extracting f, D, t : Schematics detailing the exact procedure for assigning an angle-resolved darkfield spectrum to a NP facet shape.

Fit of Au permittivity: Multipole Drude-Lorentz fit of Au used throughout this work.